PHOTONICS Research

Silicon mode-loop Mach-Zehnder modulator with L-shaped PN junction for 0.37 V·cm $V_\pi L$ high-efficiency modulation

Jiacheng Liu,[1,†] Gangqiang Zhou,[1,†] Jiangbing Du,[1,2,*] Weihong Shen,[1] Linjie Zhou,[1] and Zuyuan He[1,2]

[1]State Key Laboratory of Advanced Optical Communication Systems and Networks, Shanghai Jiao Tong University, Shanghai 200240, China
[2]Peng Cheng Laboratory, Shenzhen 518055, China
*Corresponding author: dujiangbing@sjtu.edu.cn

Received 15 September 2021; revised 25 October 2021; accepted 8 November 2021; posted 11 November 2021 (Doc. ID 442699); published 21 December 2021

Optical signaling without a high voltage driver for electric-optic modulation is in high demand to reduce power consumption, packaging complexity, and cost. In this work, we propose and experimentally demonstrate a silicon mode-loop Mach–Zehnder modulator (ML-MZM) with record-high modulation efficiency. We used a mode-loop structure to recycle light twice in the phase shifter. With an L-shaped PN junction, a comparably large overlap between the PN junction and optical modes of both TE_0 and TE_1 was achieved to lower the driving voltage or decrease the photonic device size. Proof-of-concept high-efficiency modulation with low $V_\pi L$ of 0.37 V · cm was obtained. Subvoltage V_π can be realized with a millimeter's length phase shifter by this scheme, which makes the realization of CMOS-compatible driverless modulation highly possible. 40 Gb/s signaling with a bit error rate below the 7% forward-error-correction threshold was then demonstrated with the fabricated ML-MZM, indicating great potential for high-speed optical communication.

https://doi.org/10.1364/PRJ.442699

1. INTRODUCTION

The electro-optic (EO) modulator, which translates high-speed electronic signals into the optical domain, is the key device in optical signaling systems for broad applications, including optical communication, optical sensing, and so on. Since the first demonstration of an integrated silicon photonics modulator with gigahertz (GHz) modulation frequencies in 2004 [1], substantial efforts have been made for realizing an integrated EO modulator on various photonic platforms, including indium phosphide [2], polymer [3], plasmonic [4], and lithium niobate [5]. Nonetheless, in recent years, the silicon photonics platform is broadly considered as one of the most potentially useful photonic integrated platforms because of its unique advantages such as low cost, high refractive index contrast, and CMOS-compatible fabrication process [6]. A silicon modulator with high-power efficiency and high speed is a key building block of a silicon photonics platform. To push forward the practical application of the silicon modulator, high-efficiency EO modulation with a subvoltage-level of electric driving is highly desirable for realizing CMOS-compatible driverless signaling, which is highly valuable for reducing power consumption, packaging complexity, and cost.

Currently, the Mach–Zehnder modulator (MZM) and microring modulator (MRM) are the two main kinds of widely used modulators. MRMs have a compact footprint while suffering from high temperature and fabrication sensitivity [7]. So far, high-speed silicon MRMs with data rates up to 128 Gb/s have been reported [8]. Compared with MRMs, MZMs are optically broadband and limited mainly by the bandwidth of the splitter/combiner. During the past few years, much research has been done to increase the EO bandwidth and the modulation efficiency of the MZM for dense integration. On the one hand, high-speed MZMs with data rates up to 120 Gb/s [9] and 240 Gb/s [10] have been reported by using on–off keying (OOK) modulation and six-level pulse-amplitude-modulation (PAM-6). On the other hand, modulation efficiency is still highly limited for MZM. Because of their weak phase modulation efficiency, a long phase shifter is often required for MZMs. Yet, several silicon MZMs with leading high-modulation efficiency were reported using a U-shaped PN junction with 0.51 V · cm $V_\pi L$ at C-band [11] and 0.46 V · cm $V_\pi L$ at O-band [12], using an interdigitated PN junction with 0.62 V · cm $V_\pi L$ [13], using an L-shaped PN junction with 0.81 V · cm $V_\pi L$ [14], or utilizing a folded phase shifter

with 0.72 V · cm $V_\pi L$ [15–17]. Further improvement of modulation efficiency is still needed for achieving CMOS-compatible driverless optical signaling.

In this work, we present what we believe is a novel silicon mode loop Mach–Zehnder modulator (ML-MZM) to recycle light twice as different modes within a multimode phase shifter. Mode conversion was realized by utilizing two asymmetric directional couplers (ADCs). An L-shaped PN junction was integrated in the cross section of the multimode waveguide, which modulates both the TE_0 mode and the TE_1 mode with high efficiency due to the large overlap between the PN junction and optical modes. Up to 40 Gb/s (discrete multi-tone) DMT modulation with record low $V_\pi L$ of 0.37 V · cm was demonstrated in a 1-mm long device. With the proposed L-shaped PN junction and a light recycle phase shifter, our device is more power-efficient and compact than the regular silicon MZM. By utilizing mode modes for more times of recycling, further increased modulation efficiency can be expected.

2. PRINCIPLE AND MODULATOR STRUCTURE

Figure 1 shows the schematic structure of the proposed ML-MZM device. The modulator was designed on a conventional silicon-on-insulator (SOI) wafer with a 220-nm top silicon layer and 2-μm buried oxide. It is shown that the modulator is composed of two 3-dB power splitters, four mode converters, and two multimode waveguides, supporting TE_0 and TE_1 modes.

The operating principle of the modulator is depicted in Fig. 2(a). The input light is first split equally into two branches by the multimode interferometer (MMI) 3-dB power splitter and then propagates through the multimode waveguide in TE_0 mode. The TE_0 mode loops back to the start of the multimode waveguide through the racetrack waveguide structure and converts to TE_1 mode through a tapered ADC mode converter. Afterwards, the light propagates in the TE_1 mode and passes the multimode waveguide for the second time. At the end of the multimode waveguide, the TE_1 mode is finally converted back to TE_0 mode through another ADC mode converter. The two light branches finally interfere in the MMI power combiner. The electric field intensity profiles of the TE_0 mode and the TE_1 mode are also shown in Fig. 2(a). Both of the TE_0 and the TE_1 modes are phase-modulated in the multimode waveguide by an L-shaped PN junction with high modulation efficiency.

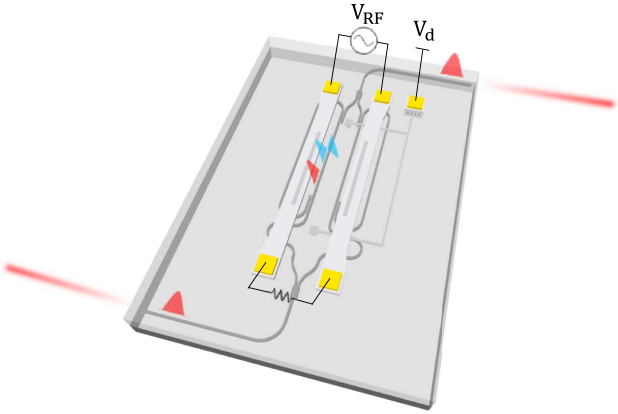

Fig. 1. Schematic structure of the ML-MZM.

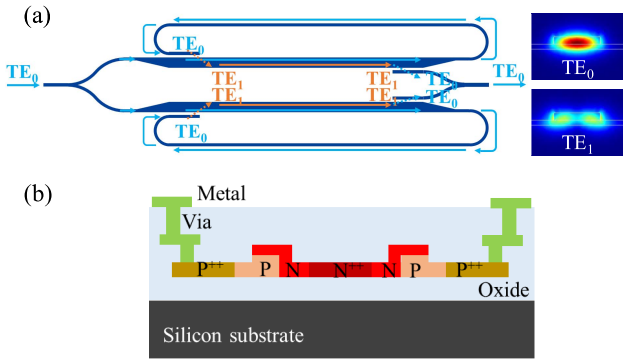

Fig. 2. (a) Operating principle of the proposed modulator; (b) cross section structure of the modulator arms.

Figure 2(b) shows the cross-sectional structure of the modulation arms. The multimode waveguide width is 840 nm, and the height is 220 nm with a 90-nm slab. The L-shaped PN junction is formed in the cross section of the multimode waveguide. The doping concentration is 1×10^{18} cm^{-3} for the p-type region and 8×10^{17} cm^{-3} for the n-type region. The heavily doped n-type and p-type concentrations are 1×10^{20} cm^{-3}. We adopt a single-drive push–pull traveling-wave electrode (TWE) design for high-speed modulation. The length of the multimode phase shifter is 1 mm.

For the proposed ML-MZM, the mode converter is of vital importance. A good mode converter should achieve mode conversion between TE_0 and TE_1 modes with high efficiency and low-mode cross talk. The most common structure of mode converter is based on the ADC for its simple structure and broadband operation. Figure 3(a) shows the top view of the designed ADC. The upper waveguide has a width varying from 0.45 to 0.2 μm, while the width of the bottom waveguide increases from 0.57 to 0.82 μm. The coupling length is 200 μm, and the coupling gap is 0.2 μm. Simulation of the ADC structure was carried out using Lumerical-FDTD Solutions, and the simulated electrical field is shown in Fig. 3(b). The calculated spectral response of the ADC is shown in Fig. 3(c). We can see that the ADC can achieve high coupling efficiency (CE) with insertion loss lower than 0.05 dB. In addition, the cross talk (XT) of the TE_0 mode is under −25 dB in the span of 1500–1600 nm.

Ideally, based on our original idea, the light will pass the phase shifter in the TE_0 mode first, then convert to the TE_1 mode, and pass the phase shifter for the second time. Therefore, the modulation efficiency of the proposed modulator should be twice that of a normal MZM. However, from our further study, we found that whether the proposed modulator can achieve the desired modulation efficiency largely depends on the PN junction structure of the phase shifter. For example, if a lateral PN junction is used in the phase shifter [shown in Fig. 4(a)], the refractive index variation of the TE_0 mode in a two-mode waveguide is lower than that of the TE_0 mode in a single-mode waveguide. Meanwhile, the sum of refractive index modulation for the TE_0 and TE_1 modes in a two-mode

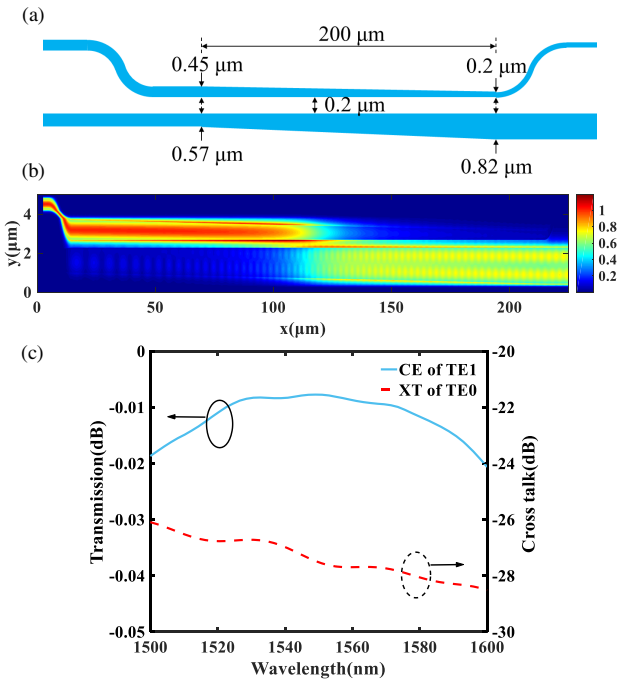

Fig. 3. (a) Top view of the designed ADC mode converter; (b) simulated electric field of ADC; (c) calculated CE and XT of the mode converter.

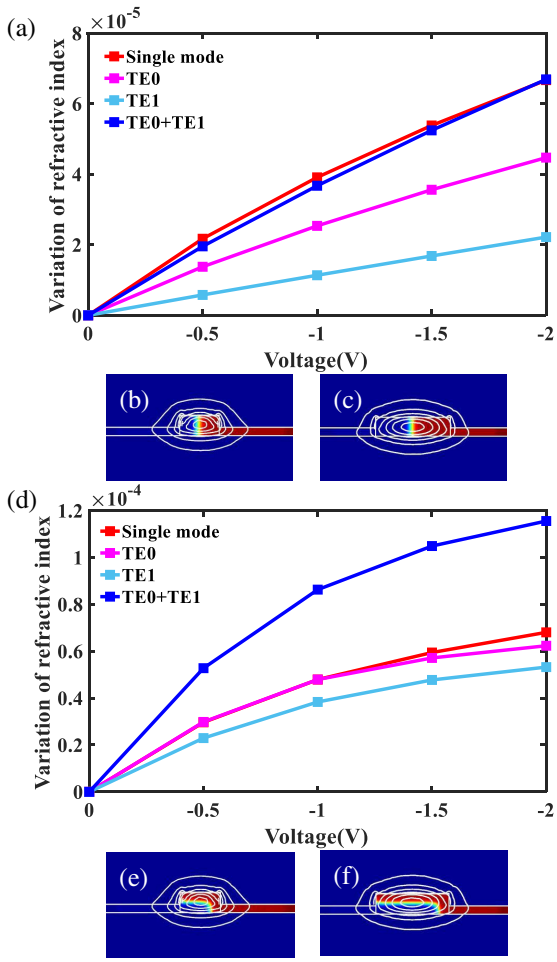

Fig. 4. (a) Refractive index variations for TE_0 and TE_1 modes as a function of reverse bias for lateral PN junction. TE_0 mode overlap with lateral PN junction of (b) single-mode waveguide and (c) two-mode waveguide. (d) Refractive index variations for TE_0 and TE_1 modes as a function of reverse bias for L-shaped PN junction. TE_0 mode overlap with L-shaped PN junction of (e) single-mode waveguide and (f) two-mode waveguide.

waveguide is almost equal to the refractive index modulation for the TE_0 mode in a single-mode waveguide. In other words, the actual enhancement of the modulation efficiency is negligible. The negligible enhancement of modulation efficiency is mainly because the required waveguide width also scales with the number of the supported modes. As the effective mode field area grows with the waveguide width, the overlap between mode profile and the PN junction will thus reduce, leading to a lower modulation efficiency in the multimode waveguide for TE_0 mode. The TE_0 mode overlap with the lateral PN junction of the single-mode waveguide and two-mode waveguide is shown in Figs. 4(b) and 4(c), respectively.

To solve the problem mentioned above, the volume of the region in which the refractive index change occurs must be increased simultaneously with the waveguide width. In other words, a horizontally placed PN junction is necessary. We numerically compared the modulation efficiency of a single-mode waveguide and a two-mode waveguide with an L-shaped PN junction to verify this conclusion. As indicated, the depletion region of an L-shaped PN junction grows with the waveguide width for the two-mode waveguide. The refractive index variation result is shown in Fig. 4(d). The TE_0 mode overlap with the L-shaped PN junction of the single-mode waveguide and the two-mode waveguide is shown in Figs. 4(e) and 4(f), respectively. We can see that, by using an L-shaped PN junction, the modulation efficiency of the TE_0 mode in the two-mode waveguide is close to that in the single-mode waveguide. The sum of refractive index modulation for the TE_0 and TE_1 modes is nearly twice that of the refractive index modulation for a TE_0 mode in a single-mode waveguide, which is consistent with our original idea. As a result, an L-shaped PN junction was finally chosen in our modulator structure. Note that we performed simulations considering an estimated doping concentration of 2.5×10^{17} cm^{-3} for the p-type region and 1.5×10^{17} cm^{-3} for the n-type region. The widths of the simulated single-mode and two-mode waveguides are 0.45 and 0.84 μm, respectively.

3. DEVICE CHARACTERIZATION

Based on the aforementioned modulator design, the device is fabricated via a standard silicon photonic processing project provided by Advanced Micro Foundry (AMF). The top silicon layer is 220 nm, and the buried oxide thickness is 2 μm. The microscope image of the fabricated modulator is shown in Fig. 5.

The static transmission spectrum under different reverse bias voltages was first measured by using a broadband optical source and an optical spectrum analyzer (OSA); the result is

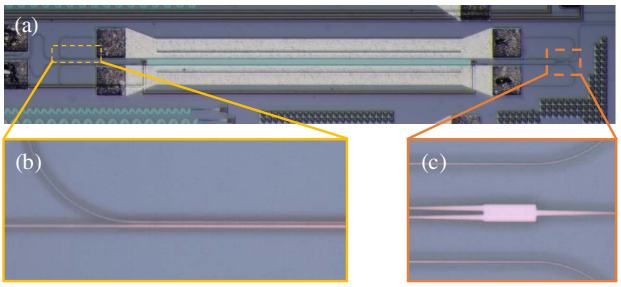

Fig. 5. Optical microscope image of (a) the fabricated ML-MZM, (b) the mode converter, (c) MMI.

shown in Fig. 6(a). The minimum transmission loss of the MZM is 24 dB (including 8 dB loss from the optical interface of the edge coupler), which mainly results from the large overlap between the optical mode field and the spatial charge region, especially for the TE_1 mode, as its mode field extends more widely and thus leads to higher absorption from the highly doped region. The static extinction ratio (ER) exceeds 10 dB and could be further improved by optimizing the MMI for an equal power split ratio. The π phase shift is achieved at a reverse bias voltage of 3.7 V, as shown in Fig. 6(b), corresponding to a $V_\pi L$ of 0.37 V · cm. The small-signal $V_\pi L$ is 0.27 V · cm and 0.35 V · cm at 0 V and −1 V bias voltage, which is the lowest value for a carrier-depletion-based silicon MZM.

In order to prove the improvement of the modulation efficiency, we fabricated the ML-MZM and a normal MZM on the same chip, as is shown in Figs. 7(a) and 7(b). Both of the devices have the same doping concentration and electrode structure. In comparison, the phase shifter length is 1 mm for the ML-MZM and 2 mm for the normal MZM. The transmission spectrum under different reverse bias voltages of the 2 mm normal MZM is shown in Fig. 7(c). We can see that the normal MZM has almost the same wavelength tuning spectra as the ML-MZM, which indicates the ML-MZM achieved the same phase shift with only half the size of a normal MZM, proving the doubled modulation efficiency, as expected by the concept.

Then, we carried out the frequency response measurement of the proposed modulator in terms of the EO S parameter. A 43-GHz vector network analyzer (VNA, Anritsu, MS46322B) was utilized, and the measured S21 curve was normalized to 100 MHz. The EO S21 curve at a bias voltage of −3 V of the proposed ML-MZM is shown in Fig. 8.

A limited 3-dB EO bandwidth of about 5 GHz is obtained at −3 V bias voltage. A significant dip at 10 GHz can be observed, which is the main contribution to the bandwidth limitation. We believe that this limitation is mainly due to the optic and microwave velocity mismatch by the time delay in the racetrack waveguide structure. In our design, the length of the racetrack waveguide structure depends on the phase shifter length, the mode converter length, and the racetrack radius. The velocity mismatch between the optical wave and the RF signal can be reduced by utilizing a shorter phase shifter and a smaller mode converter. The dip that appears at

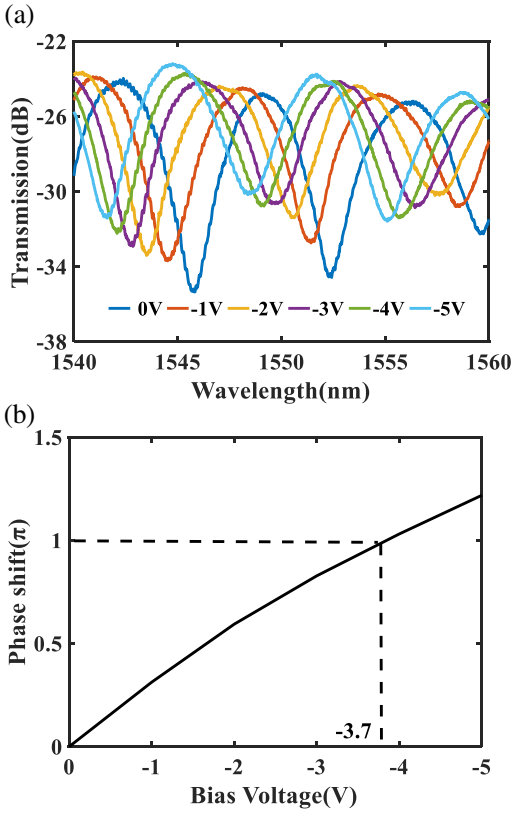

Fig. 6. (a) Transmission spectra of the ML-MZM under different reverse voltages; (b) extracted phase change as a function of bias voltage.

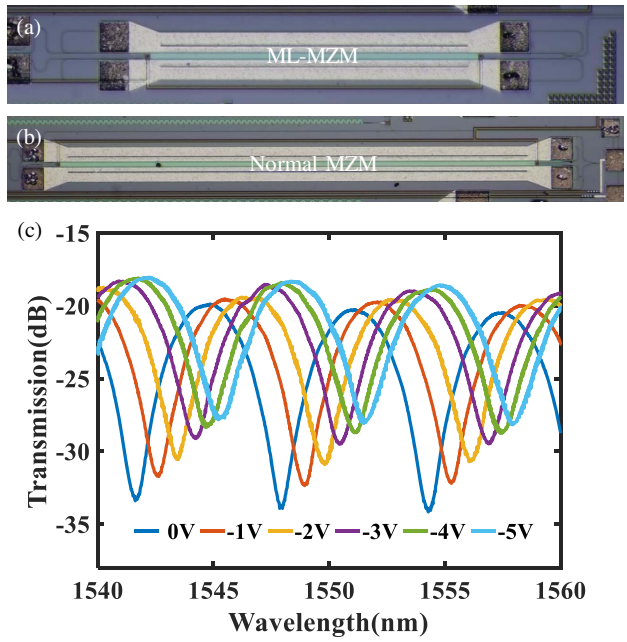

Fig. 7. (a) Microscope image of the ML-MZM with 1 mm phase shifter; (b) microscope image of the normal MZM with 2 mm phase shifter; (c) normal MZM transmission spectrum under various reverse voltages.

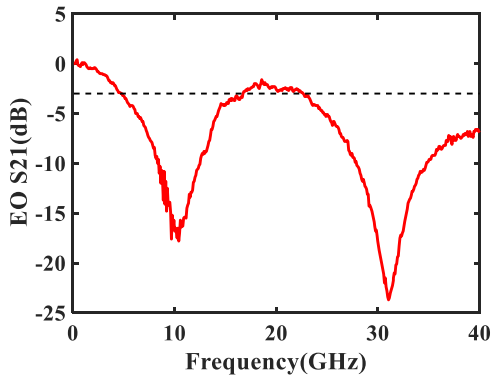

Fig. 8. Measured EO-S21 response at −3 V bias voltage.

10 GHz will move to a higher frequency, thus increasing the modulator EO bandwidth.

Figure 9(a) shows the experiment setup for high-speed modulation using the proposed modulator. A $2^7 - 1$ non-return-to-zero (NRZ) pseudo-random binary sequence (PRBS) signal was generated from a 64-GSa/s arbitrary wave generator (AWG, Keysight, M8192A) and amplified by an RF amplifier. The signal was then applied to the modulator via a 40-GHz RF probe. The end of the TWE was terminated with an external 50-Ω resistor. A −3 V bias voltage was applied to the device through a DC probe to ensure the reverse-bias condition of the PN junction. The modulated optical signal was amplified through an erbium-doped optical amplifier (EDFA) to compensate for the on-chip insertion loss and was detected by a 50-GHz photodetector. Figures 9(b) and 9(c) show the eye diagrams of the modulated OOK signals at 10 Gb/s and 15 Gb/s, respectively. The wavelength of the optical signal was set at 1569 nm. The ER is 2.91 and 2.55 dB for 10 and 15 Gb/s data rates. The limited speed of NRZ signal modulation is to be expected, based on the frequency response curve of the ML-MZM. However, one can also notice in Fig. 8 that comparably low loss of EO response can be obtained at the high-frequency band around 20 GHz, which is above the 3-dB loss threshold.

Therefore, a higher data rate can be expected by using DMT modulation format to adapt the channel response. The 40-Gb/s DMT signal with 160 subcarriers was mapped to 32 GHz bandwidth. The measured SNR response of the proposed device is plotted in Fig. 9(d). The Fischer algorithm was applied to calculate the bit allocation of the DMT signal, plotted by red circle symbols in Fig. 9(d); the calculated bit error rate (BER) curve is plotted in Fig. 9(e). The 40-Gb/s DMT signal has a BER under 7% forward-error-correction (FEC) threshold (3.8×10^{-3}) at 3-dBm received optical power. The corresponding received constellations of the four typical subcarriers are depicted in Fig. 9(f).

To characterize the high-frequency response of the modulator, we also examine the generated peak sidebands that appear under the application of modulating RF signals. The sidebands are offset from the optical carrier by an equivalent modulation frequency (5 GHz per step). A single-frequency RF signal was generated by the AWG, and the modulated optical signal is directly fed into an OSA. The intensity of the modulation sidebands is recorded for each RF frequency, as shown in Fig. 10. It can be seen that the sideband power dropped significantly at

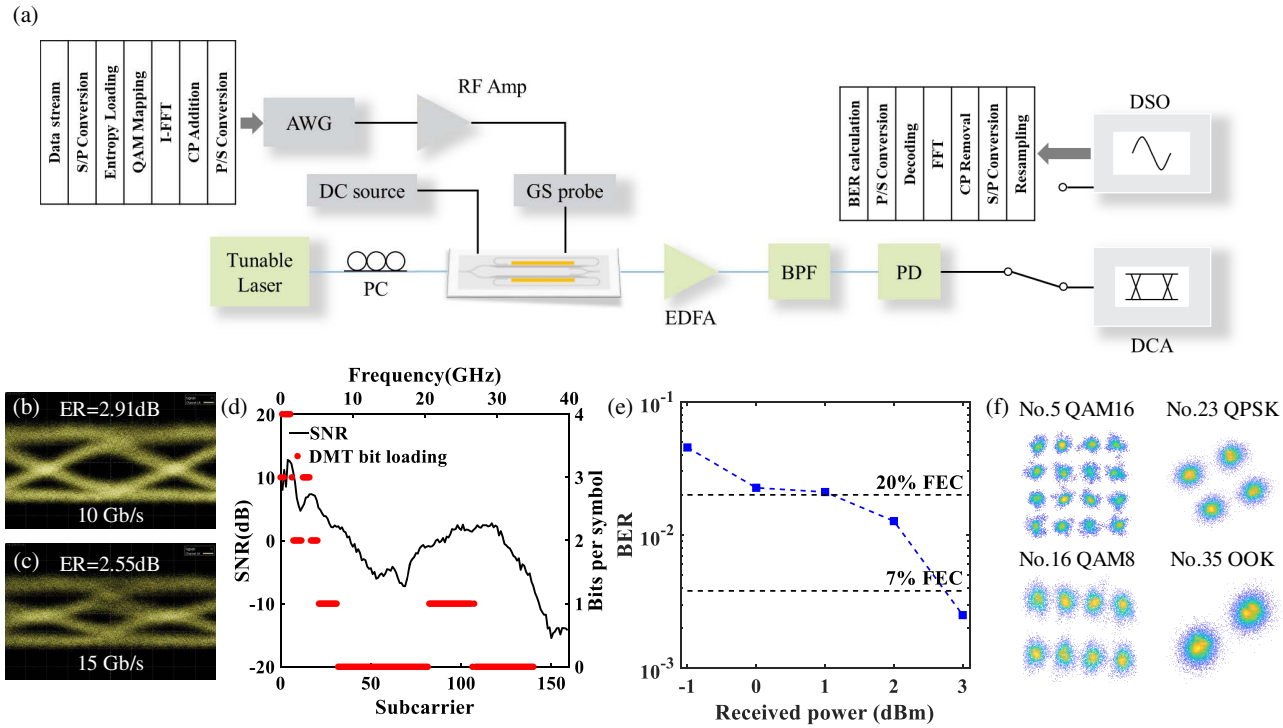

Fig. 9. (a) Schematic diagram of the high-speed measurement setup; (b) OOK eye diagram at 10 Gb/s; (c) OOK eye diagram at 15 Gb/s; (d) measured SNR response and bit allocation of 40 Gb/s DMT signal; (e) measured BER curve of 40 Gb/s DMT signal; (f) received constellations of four typical subcarriers of the DMT signal.

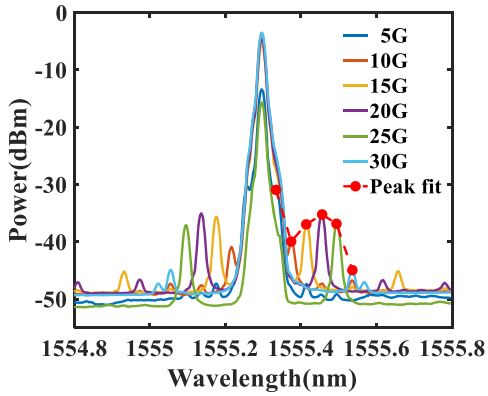

Fig. 10. Optical modulation spectra of the modulator at different RF sinusoidal frequencies.

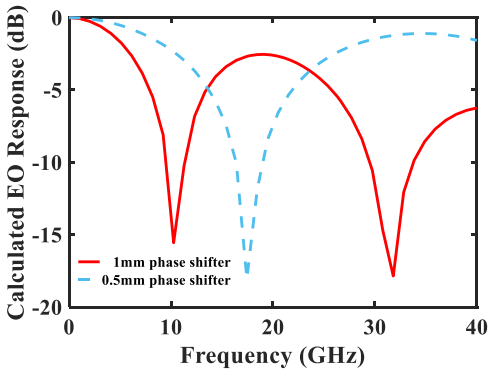

Fig. 11. Calculated EO response of ML-MZM with 1 and 0.5 mm phase shifter length.

10 GHz and reached another peak at 20 GHz. The peaks of each modulation sideband are labeled in the red fit curve, which is in good agreement with the EO S21 curve in Fig. 8. Based on these results, we believe that the proposed ML-MZM can also be used for RF tone modulation applications like high-efficiency EO frequency comb generation, which needs rather high RF voltage for generating high-order sideband tones.

4. DISCUSSION

Table 1 compares our work with state-of-the-art high modulation efficiency carrier-depletion-based silicon MZMs. It can be seen that our work possesses the highest modulation efficiency with the lowest $V_\pi L$. The high modulation efficiency can mainly be attributed to the novel structure of the multimode waveguide phase shifter and the large overlap between the L-shaped PN junction and optical modes of both TE_0 and TE_1. Besides, the working principle of the structure can also be used in a high-speed silicon modulator with U-shaped or interleaved PN junction, as long as the depletion region can increase with the width of the waveguide.

In our design, only TE_0 and TE_1 modes were used to recycle in the multimode waveguide phase shifter, considering that the capacitance of the PN junction will also grow with the waveguide width, leading to limited EO bandwidth and lower data rates. Higher-order modes could be used for more efficient phase modulation if the EO bandwidth is not limited by the width of the multimode waveguide, such as a lithium niobate waveguide. ML-MZM involving higher-order modes may have a structure similar to Ref. [18]. From the measured EO S21 curve, we can see that the sharp dip at 10 GHz significantly limits the high-speed performance of the modulator. In fact, ML-MZM is similar to the Michelson interferometer modulator (MIM) because their EO modulation bandwidths are both limited by the velocity mismatch [19]. For an ML-MZM, the velocity mismatch comes from the time delay of the racetrack loop-back waveguide. For an MIM, the velocity mismatch comes from the time delay of the reflective mirror and the counterpropagation of the optical and RF signals. Assuming negligible mode converter length and reflective mirror length, the one-time "wasted" traveling back structure in ML-MZM and counterpropagation of the optical and RF signals in MIM are the intrinsic factors which limit the EO bandwidth of both types of modulators. With reference to the theoretical equation of the MIM's modulation bandwidth in Ref. [20], we derive the theoretical equation of the ML-MZM's modulation bandwidth. We also assume that the traveling wave electrode is properly terminated and does not have any RF loss. In our simulation, the only factor that limits EO bandwidth is the velocity mismatch between optical and RF signals. For both the TE_0 and TE_1 modes, the optical signal and the RF signal are copropagating. The phase accumulation for TE_0 mode $\varphi_1(t)$ is given by

$$\varphi_1(t) = g\int_{z=0}^{L} v\left(t - n_{o1}\frac{L+M}{c} + \beta_1 z\right)\mathrm{d}z, \tag{1}$$

where $g = \pi/(LV_\pi)$, L is waveguide length of the phase shifter, and M is the total waveguide length of the loop-back structure. c is the speed of light in free space, $\beta_1 = (n_{o1} - n_m)/c$, n_{o1} is the group index of TE_0 mode, and n_m is the group index of the RF signal. The phase accumulation for TE_1 mode $\varphi_2(t)$ is given by

$$\varphi_2(t) = g\int_{z=0}^{L} v\left(t - n_{o2}\frac{L}{c} + \beta_2 z\right)\mathrm{d}z, \tag{2}$$

where $\beta_2 = (n_{o2} - n_m)/c$, and n_{o2} is the group index of the TE_1 mode. The calculated group refractive index for the TE_0 mode is 3.87 ($n_{o1} = 3.87$) and for the TE_1 mode is 4.08 ($n_{o2} = 4.08$). The calculated effective refractive index of

Table 1. Performance Comparison of Carrier-Depletion-Based Silicon Interferometric Modulator

Reference	Structure	Operation Band	Bandwidth (GHz)	$V_\pi L$ (V · cm)	Speed (Gb/s)
[11]	MZM	C-band	14.7	0.51	64
[12]	MZM	O-band	13	0.46	24
[13]	MZM	C-band	2.6	0.62	10
[14]	MZM	C-band	12	0.81	10
[16]	MIM	C-band	12	0.86	30
[15]	MIM	C-band	11.3	0.72	40
[17]	MIM	C-band	12	0.95	40
This work	ML-MZM	C-band	5	0.37	40

the microwave is about 6.57 ($n_m = 6.57$ at 20 GHz). Introducing the RF signal $v(t) = v_0 \cos(\Omega t)$ to Eqs. (1) and (2), we have

$$\varphi_1(t) = gLv_0 \mathrm{sinc}\left(\frac{\Omega\beta_1 L}{2\pi}\right) \cos\left[\Omega\left(t - n_{o1}\frac{L+M}{c} + \frac{\beta_1 L}{2}\right)\right], \tag{3}$$

$$\varphi_2(t) = gLv_0 \mathrm{sinc}\left(\frac{\Omega\beta_2 L}{2\pi}\right) \cos\left[\Omega\left(t - n_{o2}\frac{L}{c} + \frac{\beta_2 L}{2}\right)\right]. \tag{4}$$

Thus, we got the total phase shift $\varphi(t)$ given by

$$\varphi(t) = \varphi_1(t) + \varphi_2(t) = gLv_0[A\ \sin(\Omega t) + B\ \sin(\Omega t + \theta)], \tag{5}$$

$$\varphi(t) = gLv_0 C(\Omega) \sin[\Omega t + \varphi(\Omega)], \tag{6}$$

where $A = \mathrm{sinc}[\Omega\beta_1 L/(2\pi)]$, $B = \mathrm{sinc}[\Omega\beta_2 L/(2\pi)]$, $C(\Omega) = \sqrt{A^2 + B^2 + 2AB\cos\theta}$, and $\theta = \Omega\left[n_{o1}\frac{L+M}{c} - n_{o2}\frac{L}{c} + \frac{L}{2}(\beta_2 - \beta_1)\right]$. The EO response spectrum is then given by

$$S_{\mathrm{EO}}(\Omega) = \frac{J_1[2L \cdot C(\Omega)]}{J_1[2L \cdot C(0)]}, \tag{7}$$

where $J_1[\cdot]$ is the first-order Bessel function of the first kind.

For the proposed ML-MZM, L is 1 mm and M is 2.69 mm. The calculated EO response of the proposed ML-MZM is shown in Fig. 11 with a red solid curve, which is consistent with the experiment result shown in Fig. 8. The velocity mismatch comes from the time delay of the racetrack loop-back waveguide, and it can be reduced by structures with shorter phase shifter length and smaller mode converter. Taking an ML-MZM with 0.5-mm phase shifter length as an example, the 3-dB EO bandwidth can be further increased to 11.3 GHz, as is shown in Fig. 11 by the blue dashed curve.

5. CONCLUSION

We proposed and experimentally demonstrated a silicon ML-MZM for recycled electric-optic modulation. High modulation efficiency with low $V_\pi L$ of 0.37 V · cm was obtained, mainly attributed to the novel structure of the multimode waveguide phase shifter and the large overlap between the two optical modes and the L-shaped PN junction. The preliminary measurement shows that the modulator can realize 15 Gb/s OOK modulation. A relatively high data rate of up to 40 Gb/s was achieved by DMT modulation for adapting the RF response, with a dip at 10 GHz. This proof-of-concept study of ML-MZM is of great significance for pushing forward the application of silicon photonics towards CMOS-compatible driverless signaling and small footprint photonic integration.

Funding. National Key Research and Development Program of China (2018YFB1801004); National Natural Science Foundation of China (61875049, 61875124, 61935011); The Major Key Project of PCL (PCL2021A14).

Disclosures. The authors declare no conflicts of interest.

†These authors contributed equally to this paper.

REFERENCES

1. A. Liu, R. Jones, L. Liao, D. Samara-Rubio, D. Rubin, O. Cohen, R. Nicolaescu, and M. Paniccia, "A high-speed silicon optical modulator based on a metal–oxide–semiconductor capacitor," Nature **427**, 615–618 (2004).
2. Y. Ogiso, J. Ozaki, Y. Ueda, N. Kashio, N. Kikuchi, E. Yamada, H. Tanobe, S. Kanazawa, H. Yamazaki, Y. Ohiso, T. Fujii, and M. Kohtoku, "Over 67 GHz bandwidth and 1.5 V V_π InP-based optical IQ modulator with n-i-p-n heterostructure," J. Lightwave Technol. **35**, 1450–1455 (2016).
3. S. Wolf, H. Zwickel, C. Kieninger, M. Lauermann, W. Hartmann, Y. Kutuvantavida, W. Freude, S. Randel, and C. Koos, "Coherent modulation up to 100 GBd 16QAM using silicon-organic hybrid (SOH) devices," Opt. Express **26**, 220–232 (2018).
4. M. Ayata, Y. Fedoryshyn, W. Heni, B. Baeuerle, A. Josten, M. Zahner, U. Koch, Y. Salamin, C. Hoessbacher, C. Haffner, D. L. Elder, L. R. Dalton, and J. Leuthold, "High-speed plasmonic modulator in a single metal layer," Science **358**, 630–632 (2017).
5. C. Wang, M. Zhang, X. Chen, M. Bertrand, A. Shams-Ansari, S. Chandrasekhar, P. Winzer, and M. Lončar, "Integrated lithium niobate electro-optic modulators operating at CMOS-compatible voltages," Nature **562**, 101–104 (2018).
6. G. T. Reed, G. Mashanovich, F. Y. Gardes, and D. Thomson, "Silicon optical modulators," Nat. Photonics **4**, 518–526 (2010).
7. A. Rahim, A. Hermans, B. Wohlfeil, D. Petousi, B. Kuyken, D. Van Thourhout, and R. Baets, "Taking silicon photonics modulators to a higher performance level: state-of-the-art and a review of new technologies," Adv. Photon. **3**, 024003 (2021).
8. J. Sun, R. Kumar, M. Sakib, J. B. Driscoll, H. Jayatilleka, and H. Rong, "A 128 Gb/s PAM4 silicon microring modulator with integrated thermo-optic resonance tuning," J. Lightwave Technol. **37**, 110–115 (2019).
9. H. Zhang, M. Li, Y. Zhang, D. Zhang, Q. Liao, J. He, S. Hu, B. Zhang, L. Wang, X. Xiao, N. Qi, and S. Yu, "800 Gbit/s transmission over 1 km single-mode fiber using a four-channel silicon photonic transmitter," Photon. Res. **8**, 1776–1782 (2020).
10. M. Jacques, Z. Xing, A. Samani, E. El-Fiky, X. Li, M. Xiang, S. Lessard, and D. V. Plant, "240 Gbit/s silicon photonic Mach-Zehnder modulator enabled by two 2.3-Vpp drivers," J. Lightwave Technol. **38**, 2877–2885 (2020).
11. G. Zhou, L. Zhou, Y. Guo, S. Chen, L. Lu, L. Liu, and J. Chen, "32-Gb/s OOK and 64-Gb/s PAM-4 modulation using a single-drive silicon Mach–Zehnder modulator with 2 V drive voltage," IEEE Photon. J. **11**, 6603610 (2019).
12. Z. Yong, W. D. Sacher, Y. Huang, J. C. Mikkelsen, Y. Yang, X. Luo, P. Dumais, D. Goodwill, H. Bahrami, P. G.-Q. Lo, E. Bernier, and J. K. S. Poon, "U-shaped PN junctions for efficient silicon Mach-Zehnder and microring modulators in the O-band," Opt. Express **25**, 8425–8439 (2017).
13. H. Yu, M. Pantouvaki, J. V. Campenhout, D. Korn, K. Komorowska, P. Dumon, Y. Li, P. Verheyen, P. Absil, L. Alloatti, D. Hillerkuss, J. Leuthold, R. Baets, and W. Bogaerts, "Performance tradeoff between lateral and interdigitated doping patterns for high speed carrier-depletion based silicon modulators," Opt. Express **20**, 12926–12938 (2012).
14. K. Goi, N. Ishikura, H. Ishihara, S. Sakamoto, K. Ogawa, T.-Y. Liow, X. Tu, G.-Q. Lo, and D.-L. Kwong, "Low-voltage silicon Mach-Zehnder modulator operating at high temperatures without thermo-electric cooling," in *Optical Fiber Communication Conference* (2016), paper W2A-23.
15. D. Patel, V. Veerasubramanian, S. Ghosh, A. Samani, Q. Zhong, and D. V. Plant, "High-speed compact silicon photonic Michelson interferometric modulator," Opt. Express **22**, 26788–26802 (2014).
16. X. Li, X. Xiao, H. Xu, Z. Li, T. Chu, J. Yu, and Y. Yu, "Highly efficient silicon Michelson interferometer modulators," IEEE Photon. Technol. Lett. **25**, 407–409 (2013).
17. M. Wang, L. Zhou, H. Zhu, Y. Zhou, Y. Zhong, and J. Chen, "Low-loss high-extinction-ratio single-drive push-pull silicon Michelson interferometric modulator," Chin. Opt. Lett. **15**, 042501 (2017).
18. M. Lipson, S. A. Miller, C. T. Phare, Y.-C. Chang, X. Ji, O. A. J. Gordillo, A. Mohanty, S. P. Roberts, M. C. Shin, B. Stern, and M.

Zadka, "Silicon photonics integration for future generation optical network," in *European Conference on Optical Communication (ECOC)* (2018), pp. 1–2.
19. X. Huang, Y. Liu, Z. Li, H. Guan, Q. Wei, M. Tan, and Z. Li, "40 GHz high-efficiency Michelson interferometer modulator on a silicon-rich nitride and thin-film lithium niobate hybrid platform," Opt. Lett. **46**, 2811–2814 (2021).
20. J. Jian, M. Xu, L. Liu, Y. Luo, J. Zhang, L. Liu, L. Zhou, H. Chen, S. Yu, and X. Cai, "High modulation efficiency lithium niobate Michelson interferometer modulator," Opt. Express **27**, 18731–18739 (2019).